Device Simulation of SWNT-FETs

Jing Guo[1] and Mark Lundstrom[2]

[1] Department of Electrical and Computer Engineering, University of Florida, Gainesville, FL, 32611

[2] School of Electrical and Computer Engineering, Purdue University, West Lafayette, IN, 47907

1 Introduction

In recent years, significant progress in understanding the physics of carbon nanotube (CNT) electronic devices and in identifying potential applications has occurred [1, 2]. In a CNT [3, 4], low bias transport can be nearly ballistic across distances of several hundred nanometers. Deposition of high-κ gate insulators does not degrade the carrier mobility. The conduction and valence bands are symmetric, which is advantageous for complementary applications. The bandstructure is direct, which enables optical emission. Because of these attractive features, carbon nanotubes are receiving much attention for potential nanoscale field-effect transistor (FET) applications. CNTFETs also provide a concrete context for exploring mesoscopic physics of one-dimensional nanostructures.

Device simulations of CNTFETs have been extensively reported in last five years [5-16]. Significant advances have been achieved in developing simulation methods, understanding device physics, and optimizing designs using modeling and simulation. This chapter is not intended to be an extensive review of the field. We focus on the device physics of CNTFETs

To appear in *Carbon Nanotube Electronics*, edited by A. Javey and J. Kong, Springer, 2007

as revealed by quantum device simulation. The simulation results are entirely taken from the work by the authors and their collaborators.

The chapter is organized as follows. Section 2 describes an atomistic simulation approach for CNTFETs using the non-equilibrium Green's function (NEGF) formalism. Section 3 discusses device characteristics at the ballistic limit. The effect of phonon scattering on device characteristics is discussed in Section 4. Section 5 assesses the high-frequency performance limits of CNTFETs at the ballistic limit and in the presence of scattering. Section 6 examines photoconductivity of CNTFETs, and Sec. 7 summarizes this chapter.

2 SWNT-FET Simulation Using NEGF Approach

2.1 The NEGF formalism

Conventional device simulation methods treat nanoscale devices using a top-down approach by inserting quantum extensions into semiclassical transport models. For molecular scale devices, the validity of the top-down approaches is questionable. The simulation methods for molecular scale devices should incorporate an understanding of atomistic structures, quantum effects, and multi-phenomena (e.g. heat dissipation, light emission). They should also be able to treat open boundaries for devices to connect to circuits, and be computationally efficient enough for routine simulations. New bottom-up simulation methods (from atomistic level to device level) are being explored to address these challenges.

The non-equilibrium Green's function (NEGF) formalism[17-19] provides an ideal approach for bottom-up device simulations due to the following reasons, (1) atomistic descriptions of devices can be readily implemented, (2) open boundaries can be rigorously treated, and (3) multi-phenomena (e.g. inelastic scattering, AC characteristics, light emission, and etc.) can be modeled.

Figure 1 summarizes how to apply the NEGF approach to a generic transistor. The transistor channel, which can be a piece of silicon, a carbon nanotube, or a single molecule, is connected to the source and drain contacts. The channel conductance is modulated by the gate. The step-by-step procedure for the NEGF approach is described as follows [19]:.

(1) Identify a suitable basis set and write down the Hamiltonian matrix H for the isolated channel. The self-consistent potential, which is a part of the Hamiltonian matrix, is included in the diagonal components of H. The size of the N x N Hamiltonian matrix is determined by the total number of basis functions in the channel region.

(2) Compute the self-energy matrices, $\boldsymbol{\Sigma}_1$, $\boldsymbol{\Sigma}_2$, and $\boldsymbol{\Sigma}_S$, which describe how the channel couples to the source contact, the drain contact, and the dissipative processes (e.g., phonon scattering, electron-photon coupling), respectively. The source and drain self-energies can be computed using a recursive relation [19]. At the ballistic limit, $\Sigma_S = 0$. The dissipative processes can be treated by conceptually adding a “scattering contact” which in steady state takes carriers away from the initial states and put an equal number of carriers back to the final states. The carrier statistics of the “scattering contact” are determined by the distribution function of the channel, so that Σ_S needs to be iteratively solved with the Green’s function using the self-consistent Born approximation [19].

(3) Compute the retarded Green’s function,

$$G^r(E) = \left[(E + i0^+)I - H - \Sigma_1 - \Sigma_2 - \Sigma_S\right]^{-1} \tag{2.1}$$

It is computationally expensive to compute the Green’s function by directly inverting the matrix, because the inversion need to be performed for a large number of energy grid points. Efficient computational techniques, such as a recursive algorithm, have been developed to reduce the computational cost by order of magnitude[20].

(4) Determine the physical quantities of interest from the Green’s function matrix. For example, the electron density can be computed by integrating the diagonal entries of the following electron correlation function over energy,

$$G^n(E) = G^r\left[\Gamma_1 f_1(E) + \Gamma_2 f_2(E) + \Sigma_s^{in}\right] G^{r+} \tag{2.2}$$

where $f_{1,2}$ are the equilibrium Fermi functions of the two contacts, and $\Gamma_{1,2} = i(\Sigma_{1,2} - \Sigma_{1,2}^{+})$ are the broadening functions of contact 1 or contact 2, and Σ_{S}^{in} is the in-scattering function of the dissipative processes.

(5) For a self-consistent solution, the NEGF transport equation is solved iteratively with the Poisson equation until self-consistency is achieved. The source current, for example, can then be computed as

$$I_S = \left(4e/h\right)\int_{-\infty}^{+\infty} dE \cdot \mathrm{Trace}\left[\Sigma_1 f_1 A - \Gamma_1 G^n\right] \tag{2.3}$$

where $A = i(G^r - G^{r+})$ is the spectral function, and the factor of 4 comes from a spin degeneracy of 2 and a valley degeneracy of 2 in the carbon nanotube energy bandstructure.

The NEGF approach as outlined here is based on a number of simplifying assumptions such as the use of a single particle, mean field picture. See Datta for a discussion of the method [19].

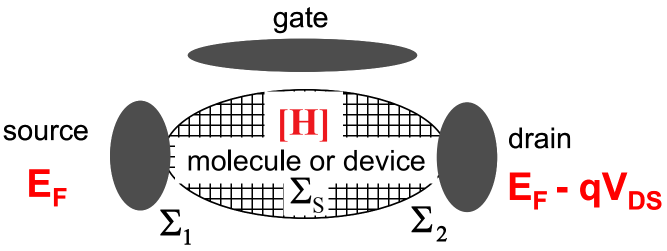

Fig. 1. A generic transistor comprised of a device channel connected to source and drain contacts. The source-drain current is modulated by a third electrode, the gate. The quantities involved in the NEGF formalism are also shown.

2.2 SWNT-FET Simulation in a Real Space Basis Set

The NEGF approach as described above can be implemented in an atomistic basis set that consists of the p_Z orbitals of all the carbon atoms in the channel. There are four orbitals in the outer electron shell of a carbon atom (s, p_x, p_y, and p_z). One p_z orbital is often sufficient because the bands involving p_z orbitals are largely uncoupled from the bands involving the other orbitals, and the bands due to the s, p_x and p_y orbitals are either well below or well above the Fermi level, and therefore, unimportant for carrier transport [4, 21]. We use a tight-binding approximation to describe the interaction between carbon atoms, and only nearest neighbor coupling with a coupling parameter of $t = 3\text{eV}$ was considered. Notice that the so-called σ-π hybridization, which can be important for very small diameter tubes (<0.8nm), is not treated in the model. The σ-π hybridization can be treated using a 4 orbital tight binding model [22], the extended Hückel theory [23], or an *ab intio* simulation [24], which is beyond the scope of this chapter.

The real space approach produces matrices in the size of the number of carbon atoms in the channel. A CNT channel with a length of tens of nanometers consists of several thousand carbon atoms. The straightforward but computationally expensive approach is to compute G^r is by directly inverting the matrix $G_{inv} = (E + i0^+)I - H - \Sigma_1 - \Sigma_2 - \Sigma_S$. Significant computational savings can be achieved by exploiting the block tridiagonal structure of G_{inv}, which allows G^r to be computed by a recursive algorithm without inverting a large matrix [25]. If the CNT channel consists of N_C carbon rings of a (n, 0) nanotube, the computational cost of directly inverting G_{inv} goes as $\mathrm{O}[(n^3 \times N_C^3)]$ whereas with the recursive algorithm it is only $\mathrm{O}(n^3 \times N_C)$. By using the recursive algorithm, the computational cost only increases *linearly* with the tube length [21, 26].

2.3 SWNT-FET Simulation in a Mode Space Basis Set

A mode-space approach that significantly reduces the size of the Hamiltonian matrix when the potential around the tube is nearly invariant has also been developed [26]. The approach decouples the two-dimensional real space CNT lattice to one-dimensional modes by performing a basis transform in the circumferential direction of the tube from the real space to the k space. The wave function in the circumferential direction of each mode is a plane wave with wave vector satisfying the periodic boundary condition. For coaxially gated CNTFETs, the potential is invariant around the CNT, and the mode space approach is exact. For the CNT, and the mode space approach is exact. For CNTFETs with planar gates, the mode space approach applies as long as the potential variation around the CNT is smaller than the spacing between the subbands. This condition is satisfied by many CNTFETs demonstrated to date because the diameter of the tube is small compared to the gate oxide thickness and the spacing between the 1st and 2nd subbands is as large as several hundreds of meVs.

The mode space approach reduces the computational cost by orders of magnitude because (i) it reduces a two-dimensional problem to a set of one-dimensional problems and (ii) only the lowest a few modes are relevant to transport and need to be treated. Routine device simulation and optimization becomes possible by using the mode space approach. In the cases when the symmetry around the tube is broken, the real space treatment becomes necessary. For example, for CNTs with atomistic vacancies or defects, the variation around the circumferential direction of the CNT is large, and the mode space approach no longer applies. A recent study based on a real space treatment showed that a single atomistic vacancy can decrease the drive current of a CNTFET by as large as 25%[27].

2.4 Treatment of Metal-CNT Contacts

Most CNTFETs demonstrated to date operate as Schottky barrier transistors. Schottky barriers (SBs) exist at the metal-CNT contacts [28]. An atomistic treatment of the metal contacts is not practical for routine device simulation, so a phenomenological treatment has been developed. In the mode space treatment, the self-energy of a mode is [19]

$$\Sigma_C(E) = \tau g_s \tau^+ , \tag{2.4}$$

where τ is the coupling between the mode and the metal contact, g_s is the surface Green's function. The contact broadening function can be computed as,

$$\Gamma_C(E) = i(\Sigma_C - \Sigma_C^+) = 2\pi\tau D_s \tau^+ \tag{2.5}$$

where D_S is the density-of-states (DOS) of the metal contact and satisfies $2\pi D_s = i(g_s - g_s^+)$ If one assumes that the density of states in metal D_S and the coupling between the mode and the contact τ are energy-independent in the energy range of interest, Eq. 2.5 can be simplified as

$$\Sigma_c = -i\alpha t\,, \tag{2.6}$$

where $t \approx 3eV$ is the C-C binding parameter, and α is a unitless parameter whose value is determined by the coupling strength between the CNT and the metal contact and the DOS of the metal contact. It can be treated as a fitting parameter, whose value is determined by best fitting between the simulation results and the measurements [29].

3 Device Characteristics at the Ballistic Limit

Significant advances have been achieved in understanding the device physics of CNTFETs. CNTFETs have been made in two ways as shown in Fig. 3.1. The first kind of CNTFETs operate like an unconventional Schottky barrier FETs (Fig. 3.1a). At low gate voltages, a potential barrier is created in the channel region, the thermionic emission (TE) current over the top of the barrier is small and the transistor is turned off. At high gate voltages, the gate modulates the tunneling current by tuning the thickness of the Schottky barrier at the source end of the channel. CNTFETs demonstrated at early stages all operate as SBFETs due to their simple fabrication process[30, 31]. CNTFETs with doped source and drain extensions, which operate like a conventional MOSFET, have been demonstrated recently[32-34]. As shown in Fig. 3.1b, the gate modulate the channel conductanc at both the off and on states. The doped source and drain extensions can be created by either electrostatic gating or chemical doping. The simpler electrostatic gating approach is good for proof of concept, but the chemical doping approach is technologically more relevant. We first discuss device physics and limitations of CNT SBFETs, and then point out potential advantages of CNT MOSFETs.

Fig. 3.2 shows the (simulated) I-V characteristics of a mid-gap CNT SBFET. The I-V characteristic is ambipolar. For $V_{GS} > V_{DS}/2$, the conduction band edge is pushed down by the gate voltage. Electrons can tunnel from the source contact into the channel region and produce electron current. For $V_{GS} < V_{DS}/2$, the valence band is lifted up by the gate voltage. Holes can tunnel from the drain contact into the valence band and produce hole current. The minimal leakage current is achieved at $V_{GS} = V_{DS}/2$, at which the electron current is equal to the hole current [35, 36]. In terms of band profile, it requires the conduction band bending at the source end of the channel to be symmetric to the valence band bending at the drain end of the channel. By considering that strong tunneling occurs in these devices because of the small effective mass and the thin barriers, the minimum leakage current of a SB CNTFET can be estimated as,

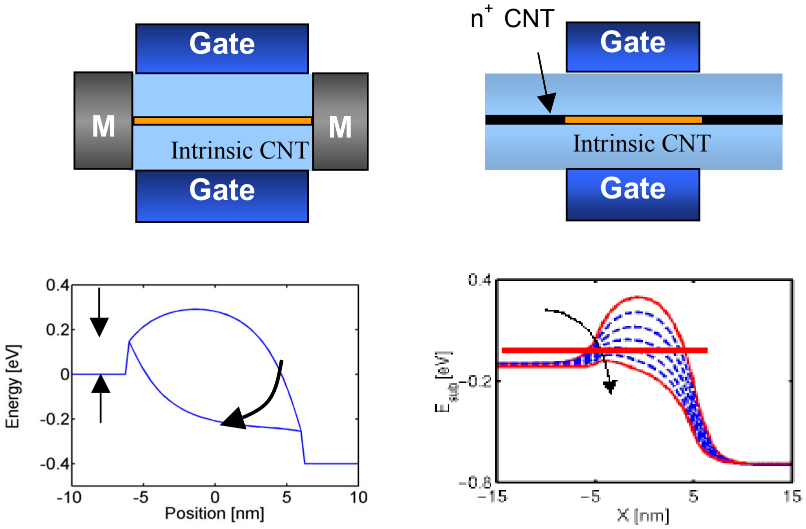

Fig.3.1 Illustration of two kinds of CNTFETs. (a) A metal source and drain FET operating as a SBFET, and (b) a FET with doped source and drain extensions operating as a MOSFET.

$$I_D = \frac{8ek_BT}{h}\langle T\rangle e^{-(E_G-qV_{DS})/2k_BT}\,, \tag{3.1}$$

where <*T*> is the average current transmission coefficient. Eq. 3.1 shows that the minimum leakage current exponentially depends on the CNT bandgap and the source-drain voltage. We next explore the scaling properties of CNT SBFETs in terms of the CNT diameter and power supply voltage.

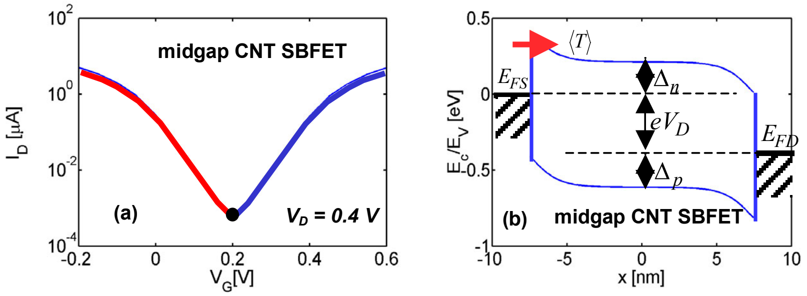

Fig.3.2 Operation of a mid-gap CNT SBFET. (a) the log (I_D) vs. V_{GS} characteristic, and (b) the energy band diagram at $V_{GS} = V_{DS}/2$.[21]

Figure 3.3 shows the I_D vs. V_G characteristics of CNT SBFETs with three different nanotube diameters. The CNT bandgap is approximately inversely proportional to the tube diameter, and can be expressed as $\sim 0.8eV/d\ (in\ nm)$ [4]. Varying the tube diameter from 1nm to 2nm changes the CNT bandgap from ~0.8eV (a value in between the Si and Ge bandgaps) to ~0.4eV (a value smaller than the Ge bandgap). Because the minimal leakage current exponentially increases as the tube diameter increases, the minimum leakage current increases dramatically as the tube diameter decreases. At the same time, the on-current is also improved because it is easier to make good contacts to materials with smaller bandgaps, but the on-off ratio decreases significantly as the nanotube diameter increases [36].

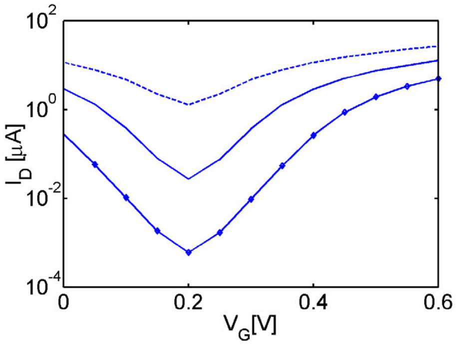

Fig.3.3 *Scaling of nanotube diameter*. I_D vs. V_G characteristics at V_D=0.4V for the CNT SBFET with different nanotube diameter. The solid line with circles is for (13,0) CNT (with d~1nm), the sold line is for (17,0) CNT (with d~1.3nm), and the dashed line is for (25,0) CNT (with d~2nm)[36].

We next examine power supply voltage scaling. Figure 3.4a shows the I_D vs. V_G characteristics of the CNT SBFET with three different power supply voltages. For each power supply voltage, we define the off-current at the minimal leakage point ($V_{G,off}=V_D/2$ and $V_D=V_{DD}$), and the on-current is defined at $V_{G,on} = V_{G,off} + V_{DD}$ and $V_D=V_{DD}$. Fig. 3.4a shows that the minimal leakage current increases exponentially as the power supply voltage increases, just as Eq. (3.1) predicts [35, 36]. Fig. 3.4a also shows that the on-current increases with V_{DD}. The off-current vs. on-current for different power supply voltages is plotted in Fig. 3.4b. The trade-off for reducing the off-current by lowering the power supply voltage is the degradation of on-current. The choice of power supply voltage will depend on the type of circuit applications.

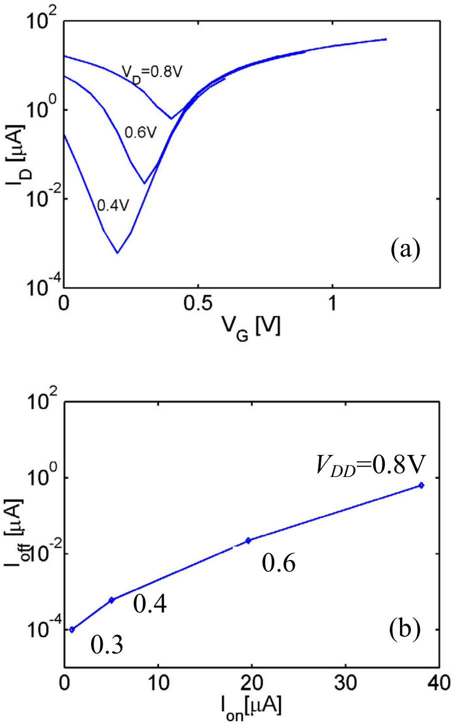

Fig.3.4 *Scaling of Power supply voltage.* (a) I_D vs V_G characteristics under different power supply voltages for the CNTFET. For each power supply voltage, the drain is biased at the power supply voltage, $V_D=V_{DD}$. (b) The off-current vs. on-current for different power supply voltages [36].

We also simulated CNT SBFETs with different metal-CNT SB heights. When the gate insulator is thin, varying the SB height has a small effect on the qualitative feature of the *I-V* curve. The transistor is ambipolar regardless of the SB height. The reason is that the SB thickness is roughly the gate oxide thickness due to electrostatic screening length [8, 37] and the effective mass of carriers in CNTs is small. The barrier is thin when the gate oxide is thin, and it is nearly transparent for any physical value of the SB height. Although the hole conduction current is larger than the elctron conduction current for a CNT SBFET with a zero SB height for holes, the transistor still qualitatively shows ambipolar characteristics when the oxide is thin (<10nm) [5, 29].

One advantage of an ambipolar CNT SBFET is that it can be used as either an n-type and p-type FET in a CMOS application if the threshold voltage of the transistor is carefully designed [38], but the large leakage current increases the standby power. Acceptable leakage currents require a bandgap of at least ~0.8eV (a nanotube diameter of less than 1 nm), but it is more difficult to make low SB contact to a CNT with a larger diameter. Carriers must tunnel into the channel at on-state, which lowers on-current. A zero SB to a CNT is possible by using a right combination of the contact material and CNT diameter [28, 39], but reducing the SB height to zero is still not enough for reaching the true ballistic performance limit at on-state, because even then a significant fraction of the current is carried by electrons below the Fermi level, which must tunnel into the semiconductor [40]. A CNT MOSFET improves both the ballistic on-current and suppresses the minimal leakage current, as shown in Fig. 3.5. For a typical MOSFET, the Fermi level in the n^+ source and at the beginning of the channel is well above the conduction band, which is effectively a negative Schottky barrier [40]. The type of doping for the source and drain extensions defines the type of the transistor and suppresses ambipolar conduction. The n^+ doped source and drain extensions do not conduct hole current. The source-drain current, however, increases when the gate voltage decreases to sufficiently negative value, which leads to band-to-band tunneling from contacts to the channel region.

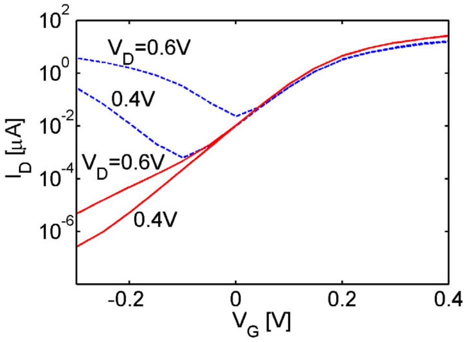

Fig. 3.5 I_D vs. V_G characteristics for the CNT MOSFET (the solid lines) and the CNT SBFET (the dashed lines) at V_D=0.4V and 0.6V.

4 Role of Phonon Scattering

The excellent carrier transport properties of CNTs have been a topic of strong interest. Since the geometry of the CNTs result in a smooth surface, surface roughness scattering can be expected to be negligible. Backscattering is suppressed by the reduction in phase space for one-dimensional conductors. The result is that mean-free-paths (mfps) of several hundred nanometers and an extraordinarily high mobility up to $20{,}000 cm^2/Vs$ are commonly observed under low bias conditions [41, 42]. Under high bias (>0.2V), however, scattering by optical phonons (OPs) and zone boundary (ZB) phonons dominates, and the mfps decrease substantially to the order of 10nm[43-45]. The effects of phonon scattering in metallic tubes and in semiconducting tubes for low-field transport (e.g., low-field mobility measurements and calculations) have been studied in literature. In this section, we focuses on high-field transport in the presence of phonon scattering in both CNT SBFETs and CNT DopoedSD-FETs[46-49].

We first perform non-self-consistent simulations to examine the direct effect of phonon scattering on the on-current of CNT SBFET [46]. The result shows that even for a channel several times longer than phonon scattering mfp, the direct effect of phonon scattering is small. For a CNTFET with an on-state conduction band profile as shown in Fig. 4.1, the ballistic on-current is computed to be 4.7μA. By using the ballistic band profile, a non-self-consistent transport simulation in the presence of phonon scattering was performed. The simulated on-current in the presence of both AP and OP/ZB scattering is I_{nsc}≈4.4µA. The current is surprisingly close to the ballistic value (~94%), although the channel length (50nm) is several times longer than the phonon scattering mfp (~10nm). A more careful examination shows that the small degradation from the ballistic current is mostly due to the near elastic AP scattering instead of the OP/ZB scattering.

Fig. 4.1 explains why the short mfp OP/ZB scattering has a small direct effect on the DC source-drain current. Electrons can tunnel into the channel from the source contact in the energy range close to the source Fermi level, as shown by the dashed line in Fig. 4.1. The source injected electrons accelerate as they travel along the channel and can possess enough energy to emit an OP/ZB phonon. After emitting an OP, whose energy is much larger in a CNT than in common semiconductors, a backscattered electron encounters a much higher and thicker Schottky barrier at the source end, and can hardly return back to the source. The result is that the electrons rattle around in the channel and finally exit to the drain. The OP and ZB scattering, though occurs even in a short-channel CNTFET, has a small direct effect on the current under modest gate biases[47].

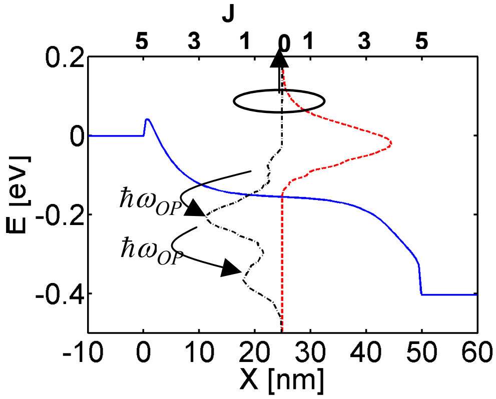

Fig.4.1 The non-self-consistently computed source current spectrum (the dashed line) and the drain one (the dash-dot line) in the presence of phonon scatterings. The first subband profile of the simulated CNT SBFET is shown by the solid line[46].

In order to describe the indirect effect of phonon scattering through self-consistent electrostatics [50], we next show self-consistent simulation results. The simulated device is a planar gate CNTFET with a 50nm-long channel and a 8nm-thick HfO_2 top gate insulator. Figure 4.2a shows that phonon scattering results in larger electron density in the channel region. The reason is that phonon scattering lowers the average carrier velocity, so the charge density in the channel must increase to maintain a similar source-drain current. Due to the self-consistent potential produced by the larger electron density, the band profile in the channel region moves up, as shown in Fig. 4.2b. The source-drain current is reduced through self-consistent electrostatics. As shown by the current spectrums plotted in Fig. 4.2b, compared to the non-self-consistently computed current spectrum (the dash-dot line), the self-consistently computed current spectrum (the solid line) delivers a smaller current density in a narrower energy window. The self-consistently computed on-current is $I_{sc} \approx 3.7\mu A$, and is about 80% of the ballistic on-current. In summary, the direct effect of scattering reduces the ballistic current by 6%, but the indirect effect reduces it by an additional 14%.

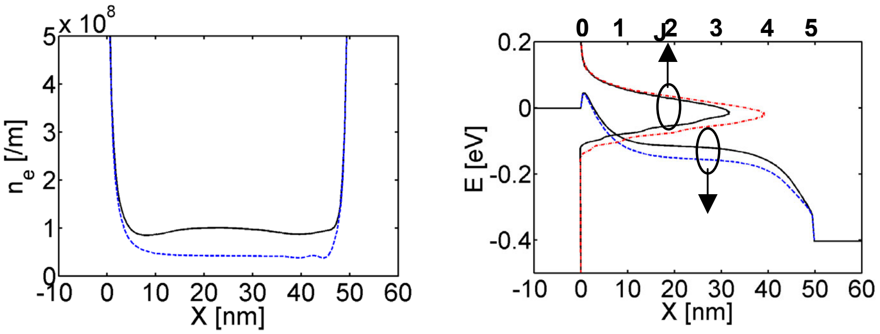

Fig.4.2 The indirect effect of phonon scattering through self-consistent electrostatics (a) The electron densities and (b) the first conduction subband profiles at the ballistic limit (the dashed lines) and in the presence of phonon scattering (the solid lines). The top axis in (b) shows the current spectrum calculated in the presence of phonon scattering. The solid line shows the self-consistently computed current spectrum (using the solid band profile). For comparison, the dash-dot line shows the non-self-consistently computed current spectrum (using the dashed band profile).

The strength of the indirect effect strongly depends on the effectiveness of gate control. For a CNTFET with thin, high-κ gate insulator, the gate insulator capacitance is larger. The self-consistent potential produced by the charge in the channel region is small, and the indirect effect is also small. On the other hand, For a CNTFET with thick gate insulator and a small gate capacitance, the self-consistent potential produced by the charge in the channel is larger. The indirect effect through self-consistent electrostatics is also more important.

The indirect effect of phonon scattering also occurs in a CNT MOSFET. Figures 4.3a and 4.3b sketch the subband profile and an OP emission event under a modest gate bias in a CNT SBFET and in a CNT MOSFET, respectively. For the CNT SBFET, the current is controlled by quantum tunneling through the Schottky barrier at the source end of the channel. For the CNT MOSFET, the current is controlled by thermionic emission over the top of the barrier at the beginning of the channel. For both transistors, OP/ZB phonon scattering can result in pile-up of charge in the channel, and affects the potential profile near the source through two-dimensional electrostatic effect. The indirect effect in the CNT SBFET, however, is expected to be more severe than in the CNT MOSFET. As shown in Fig. 4.3, the potential profile at the beginning of the channel in the CNT SBFET varies much more rapidly than in the CNT MOSFET. As a result, the source-injected electrons in the CNT SBFET can gain enough energy and emit an optical phonon within a distance much shorter than that in the CNT MOSFET. The pile-up of charge in a CNT SBFET occurs closer to the beginning of the channel, and has a larger effect on the potential profile at the beginning of the channel, which controls the source-drain current. The indirect effect, therefore, is expected to be more important in the CNT SBFET.

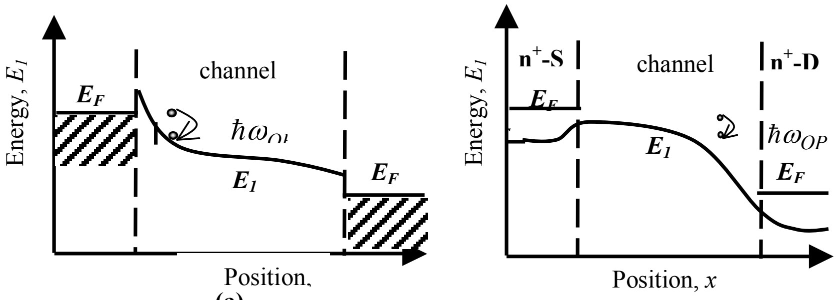

(a) **(b)**

Fig. 4.3 The schematic sketch of the first subband profile and an OP emission event for (a) a SBFET and (b) a MOSFET with a similar channel length and on-current under a modest gate bias [46].

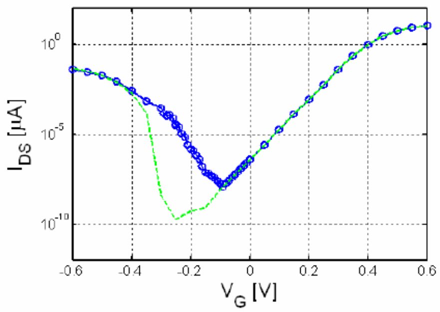

Fig.4.4 The I_D vs. V_G characteristics at V_D=0.1V for the CNT MOSFET at the ballistic limit (the dashed line) and in the presence of phonon scattering (the solid line with circles) [49].

It is also interesting to examine the effect of phonon scattering on the DC off-current of the FETs. We found that phonon scattering has a small effect on the minimal leakage current of the CNT SBFET, but significantly affect the minimal leakage current of the CNT MOSFET, as shown in Fig. 4.4. In the presence of phonon scattering, the minimal leakage current is much larger and occurs at a larger gate voltage [49]. The reason is explained in Fig. 4.5. As the gate voltage decreases, the source-drain current first exponentially decreases in the subthreshold region. As the gate voltage is sufficiently negative, the source-drain current reaches a minimum value and then exponentially increases due to the onset of band-to-band tunneling. At the ballistic limit, band-to-band tunneling occurs when the valence band in the channel aligns with the conduction band in the source extension, as shown in Fig. 4.5a. In the presence of phonon scattering, band-to-band tunneling starts to play an important before the valence band in the channel aligns with the conduction band in the source extension as gate voltage decreases due to a phonon-assisted tunneling process, as shown in Fig. 4.5b. The minimal leakage current, therefore, is reached at a larger gate voltage. The results indicate that it is important to treat phonon-assisted scattering in order to accurately compute the minimal leakage current. The steep subthreshold slope in the band-to-band tunneling current promises a new type of transistor with a subthreshold swing less than 60mV/dec [5]. Phonon-assisted tunneling again plays an important role on determining the exact value of the subthreshold slope for the band-to-band tunneling current.

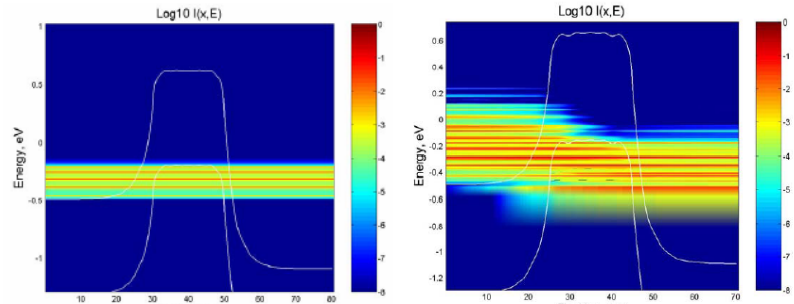

(a) (b)

Fig. 4.5. The current spectrum at the minimal bias point (a) for the ballistic limit and (b) in the presence of phonon scattering. The conduction and valence subband profiles of the CNT MOSFET are also shown[49].

5 High-Frequency Performance Limits

The excellent carrier transport properties of CNTs lead to strong interest for high-speed device applications. The low-field mobility is as high as 20,000cm^2/Vs [42, 51]. In addition, the CNTFET also provides a concrete context to study time-dependent quantum transport in one-dimensional nanostructures. The first experiments on AC characteristics were reported by Appenzeller and Frank in 2004, with a measurement frequency up to 580MHz [52, 53]. The subsequent progress has been rapid. Measurements with a frequency up to 2.6GHz [54], 10GHz [55], and 50GHz [56] have been reported. A five-stage ring oscillator built on a single tube has been demonstrated [38]. Theoretical works predict THz operation at the ballistic limit [9, 14, 57-59]. In this section, we discuss our work on assessing the high-frequency performance limits at the ballistic limit and in the presence of phonon scattering.

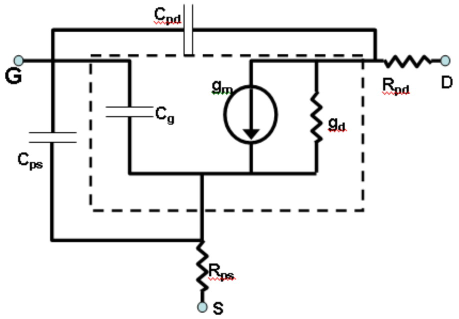

Fig. 5.1 A small-signal equivalent circuit model of a CNTFET for quasi-static simulations. The dashed rectangle shows the equivalent circuit of the intrinsic CNTFET. Parasitic capacitances and resistances are also shown [59].

Fig. 5.1 shows a small signal equivalent circuit model for a CNTFET. The high-frequency performance of a CNTFET can be assessed using the model under quasi-static approximation. The equivalent circuit model for the intrinsic CNTFET is shown within the dashed rectangle in Fig. 5.1. The parameters are obtained by running self-consistent quantum simulations and numerically evaluating the derivatives. The intrinsic gate capacitance C_g and the transconductance g_m are

$$C_g = \left.\frac{\partial Q_{ch}}{\partial V_g}\right|_{V_d} , \; g_m = \left.\frac{\partial I_d}{\partial V_g}\right|_{V_d} \tag{5.1}$$

where Q_{ch} is the total charge in the CNT channel, and I_d is the source-drain current. Here we assume that gate electrostatic control is good, so that the charge in the channel is equal to that in the gate when parasitic capacitance is zero. The source-drain conductance $g_d = \partial I_d / \partial V_d|_{V_g}$ is obtained by running DC simulations with slightly different V_d. At low V_d (linear region), $1/g_d$ accounts for the channel resistance, which includes the quantum resistance of a ballistic channel. The output conductance, g_d, is small at high V_d because the current saturates.

The parasitic capacitance between the gate and the source (drain) is treated as $C_{ps}(C_{pd})$, and the parasitic resistance of the source (drain) contact is treated as $R_{ps}(R_{pd})$. An estimation shows that the parasitic capacitance plays a more important role than the parasitic resistance in the state-of-the-art CNTFETs [14]. For a CNTFET with an equivalent circuit in Fig. 5.1, the cut-off frequency is

$$f_T \approx \frac{1}{2\pi}\frac{g_m}{C_g + C_{pS} + C_{pD}}. \tag{5.3}$$

The parasitic capacitances lower the cut-off frequency by orders of magnitude in state-of-the-art CNTFETs. In addition, parasitic resistance also imposes challenges for probing the intrinsic response of the CNTFET. The parasitic capacitance is dominant because the effective channel width (the CNT diameter) is often much smaller than the width of the contacts fabricated by microelectronic processes. Lowering the parasitic capacitance is the most important issue to improve the high-frequency performance of state-of-the-art CNTFETs. Two possible solutions to significantly reduce the effect of parasitic capacitances are (i) to fabricate a CNTFET with one-dimensional needle-like source and drain contacts, and (ii) to fabricate a CNTFET with a closely packed CNT array as the channel. To assess the performance limit, the intrinsic cut-off frequency can be computed by assuming zero parasitic capacitance,

$$f_T \approx \frac{1}{2\pi}\frac{g_m}{C_g}. \tag{5.4}$$

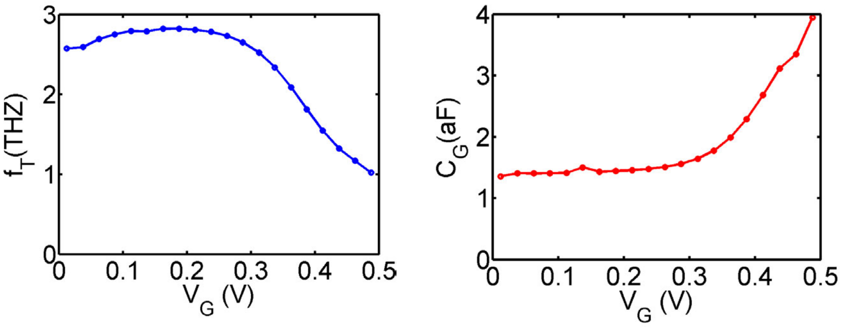

Fig.5.2 (a) The intrinsic cut-off frequency and (b) the intrinsic gate capacitance versus the gate voltage for the ballistic CNT SBFET [59]. The channel length is 50nm and the top HfO_2 gate insulator thickness is 8nm [29]. No parasitic capacitance and resistance are included.

Fig 5.2a, which plots the intrinsic cut-off frequency as a function of the gate voltage for a CNT SBFET, shows that the intrinsic cut-off frequency drops significantly as V_G increases to a large enough value. Fig. 5.2b, which plots the intrinsic gate capacitance vs. the gate voltage at V_D=V_{DD}, indicates that the drop of the cut-off frequency is due to the increase of the intrinsic gate capacitance at large V_G.

In order to understand why the gate capacitance increases at large gate overdrive in the ballistic limit, we sketch the band diagrams at a low V_G and a high V_G for a ballistic CNT SBFET, as shown in Fig. 5.3a and Fig. 5.3b, respectively. When V_G is low, only $+k$ states in the channel are occupied and contribute to the intrinsic gate capacitance because the drain injection is neglegible. In contrast, at high V_G, the first subband edge in the channel is low, and the bottom of the $-k$ states are populated due to the drain injection and reflection of soucre-injected carriers by the barrier at the drain end of the channel. As a result, the channel capacitance significantly increases when the $-k$ states at the bottom of the subband begins to be populated, where a singularity in density-of-states (DOS) exists. The cut-off frequency decreases.

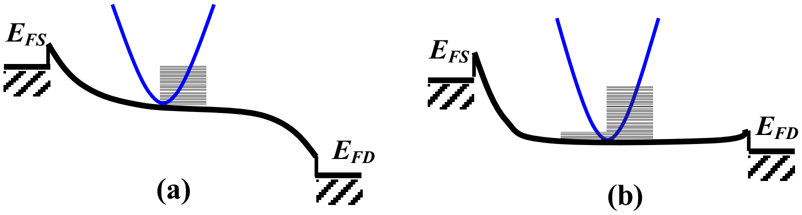

Fig.5.3 Sketch of conduction band profile at (a) a low gate overdrive and (b) a high gate overdrive for a ballistic CNT SBFET. The occupied states are covered by the gray windows

We next compare the intrinsic cut-off frequency of the ballistic CNTFET to that of a ballistic n-type Si MOSFET. Fig. 5.4, which plots the projected intrinsic cut-off frequencies vs. the transistor channel length, shows that the cut-off frequency of the CNTFET is about 50% higher than that of the n-type Si MOSFET. The larger cut-off frequency of the CNTFET at the ballistic limit is due to larger band-structure-limited velocity of the CNT channel.

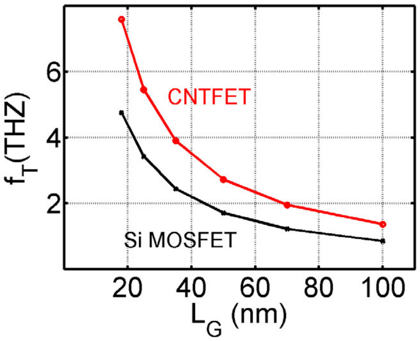

Fig.5.4 The intrinsic cut-off frequencies for the ballistic CNT SBFET and a ballistic double-gate Si MOSFET versus the channel length [59]. The performance limits are assessed and no parasitic capacitance and resistance is included.

Phonon scattering has a large effect on the intrinsic cut-off frequency of a CNT SBFET, though its direct effect on DC current is small [60]. We simulated a CNTFET with good gate electrostatic control (with a 5nm-thick, coaxial high-κ gate insulator), in which the indirect effect through self-consistent electrostatics is also small. The transconductance and on-current in the presence of phonon scattering is above 80% of the ballistic value for a channel length up to 200nm. In contrast, Fig. 5.5, which plots the intrinsic cut-off frequency versus the channel length at the ballistic limit (the circles) and in the presence of phonon scattering (the crosses), shows that phonon scattering significantly lowers f_T. The dashed line is a fitting of the ballistic result by $f_T = 110GHz \cdot \mu m / L_{ch}$, and the solid line is a fitting of the scattering result by $f_T = 40GHz \cdot \mu m / L_{ch}$. Although the transistor delivers a near ballistic DC on-current (>80%), the cut-off frequency in the presence of phonon scattering is only about 40% of the ballistic value for the simulated channel lengths. The reason is that phonon scattering leads to random walks of electrons and lowers the average carrier velocity, as shown in the inset of Fig. 5.5. The charge piles up in the channel and the intrinsic gate capacitance C_g increases significantly. The cut-off frequency, which is determined by g_m / C_g decreases mostly due to the increase of C_g.

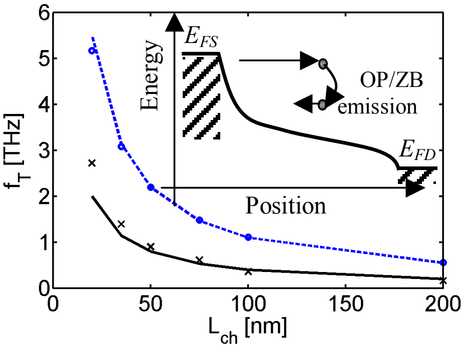

Fig.5.5 The cut-off frequency versus the channel length at on-state (V_D=V_G=0.5V). The circles are numerically computed f_T at the ballistic limit and the dashed line is a fitting curve of $f_T = 110GHz \cdot \mu m / L_{ch}$. The crosses are numerically computed f_T in the presence of phonon scattering and the solid line is a fitting curve of $f_T = 40GHz \cdot \mu m / L_{ch}$. The inset sketches a source-injected electron, which gets backscattered by emitting an OP/ZB phonon[60].

The CNTFET examined above has a thin high-κ gate insulator and a large gate insulator capacitance C_{ins}. The CNTFET operates close to the so-called quantum capacitance (C_Q) limit [61]. The indirect effect of phonon scattering through self-consistent electrostatics is small. The gate capacitance, which is the series combination of C_{ins} and C_Q, is close to the quantum capacitance because C_{ins}>C_Q. We also examined the case when the gate insulator is thick and the transistor operates close to the conventional MOSFET limit [13]. Phonon scattering does not lead to an increase of the intrinsic gate capacitance because C_{ins}<<C_Q thus $C_g \approx C_{ins}$. It does, however, severely degrade the DC source-drain current and transconductance indirectly through the self-consistent electrostatic effect. The intrinsic cut-off frequency, which is determined by g_m / C_g , still decreases, but mostly due to the decrease of g_m , instead of due to the increase of C_g .In summary, how scattering affects the performance of these devices depends not only on the physics of scattering, but also on device design.

6 Optoelectronic Phenomena

Since the first demonstration of electroluminescence (EL) from a CNTFET about three year ago [62], significant progress has been achieved in CNT optoelectronics [63-69]. The channel of the device consists of a single molecule, which makes it the smallest light emitting device demonstrated to date. Although at its early stage, the advance of CNT optoelectronics might eventually lead to important applications. In this section, we apply the NEGF approach to simulate photoconductivity of a CNT SBFET [70].

Fig. 6.1 shows the simulated device geometry. A back-gated CNT SBFET is illuminated. The light is polarized along the CNT channel. We simulate the photo-current as a function of the light intensity and photon energy. A band-to-band transition picture is used. Notice that the electrostatic binding energy of the so-called exciton (an electron-hole pair) can be large in a CNT due to its one-dimensional geometry and decreased electrostatic screening [71]. Excitons may play an important role in CNT optoelectronic devices. Although the treatment of excitons in a CNT device simulation warrants careful future studies, it is beyond the scope of this discussion.

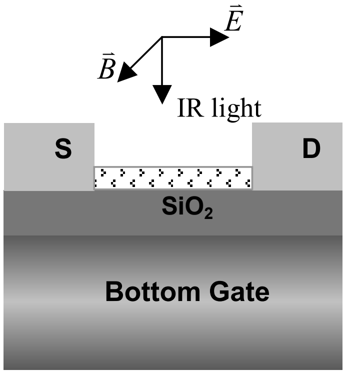

Fig.6.1 The simulated CNT SBFET under infrared (IR) light illumination. The electric field, $\vec{E}$, is polarized along the CNT channel. The intrinsic channel has a length of L_{ch}=15nm. The SiO$_2$ bottom oxide thickness is 8nm [70].

Fig. 6.2a shows the I_D-V_G characteristics of the transistor without light illumination (the solid line) and with different illumination intensities. The dark current shows a strong dependence on the gate voltage and the minimum leakage current is obtained at $V_G=V_D/2$. In contrast, the photocurrent, which is determined by the illumination intensity and the quantum efficiency, is nearly independent of the gate voltage. As the illumination intensity increases, the photocurrent becomes dominant and the dependence of I_D on V_G becomes much weaker. The source-drain current increases as the illumination intensity increases. The increases is especially obvious for bias points close to $V_G=V_D/2$, at which the dark current reaches the minimum value. The results are in qualitative agreement with the experiment on a longer channel device [64].

Figure 6.2b plots the energy and position resolved current spectrum, $J(E, x)$, under a illumination intensity of $10^7 W/cm^2$ and photon energy $\hbar\omega = 0.7eV$ at $V_G=V_D/2$. The conduction subband profile is symmetric to the valence subband profile. Absorption of a photon by an electron in the valence band creates an electron-hole pair. Because the conduction band is coupled more strongly to the drain than to the source due to the SB for electrons at the source end of the channel, electrons flow to the drain. On the other hand, because the valence band is coupled more strongly to the source due to the SB for holes at the drain end of the channel, holes flow to the source. The asymmetric couplings of electrons and holes to different contacts separate photo-generated electrons and holes, and the CNT SBFET operates as a photodetector.

We next examine the effect of phonon scattering on the photocurrent spectrum. Fig. 6.2b shows a photon-generated electron can be accelerated by the electric field. Enough kinetic energy can be gained near the drain and a OP/ZB phonon can be emitted. The backscattered electron, however, is unlikely to return back to the source because it encounters a much higher and thicker SB. Phonon scattering has a small *direct* effect on the photocurrent, but it significantly changes the energy-resolved photocurrent spectrum. At the ballistic limit, only one peak appears in the spectrum of the electron photo-current. In the presence of phonon scattering, additional peaks appear at energies of $n\hbar\omega_{OP}$ (where n is an integer) below the main peak due to OP/ZB phonon emission, as shown in Fig. 6.2b.

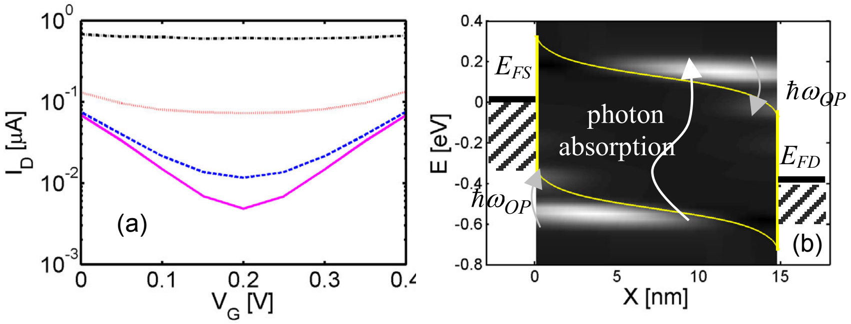

Fig.6.2 (a) I_D vs. V_G characteristics without light illumination (the solid line) and with three different illumination power densities, $10^5 W/cm^2$ (the dashed line), $10^6 W/cm^2$ (the dotted line), and $10^7 W/cm^2$ (the dash-dot line). (b) The energy and position resolved current spectrum, $J(E, x)$, on a grayscale plot at V_G=V_D/2=0.2V. A brighter color represents a larger value [70].

We next investigate how the source-drain current depends on the photon energy and the CNT diameter. Figure 6.3 plots the source-drain current versus the photon energy for three zigzag CNTs with different diameters and subband gaps. When the photon energy is low, the dominant component of the source-drain current is the dark current, which exponentially increases as the tube diameter increases [36]. Even for the photon energies below the subband gap energy, a considerable photocurrent flows due to photon-assisted tunneling [72]. (In a quantum mechanical treatment, electrons in the valence subband can absorb a phonon with an energy smaller than the subband gap, and then tunnel into the conduction band if an electric field exists.) The peak value of the source-drain current is reached when the photon energy of the light is slightly above the subband gap energies because the source/drain contact broadening and weak quantum confinement along the short CNT channel direction shift the density-of-states (DOS) peak slightly away from the subband edges.

Multiple absorption peaks appear in the infrared, visible, and ultraviolet regions for each simulated device because the quantum confinement in the circumferential direction of the CNT leads to discrete one-dimensional subbands. The absorption peaks are determined by the CNT diameter. As the CNT diameter increases, the bandgap decreases, and the absorption peaks shift to lower photon energies. The result is in agreement with the experiment [64]. The absorption wave length, therefore, can be engineered by properly choosing the CNT diameter, which offers another dimension for device design.

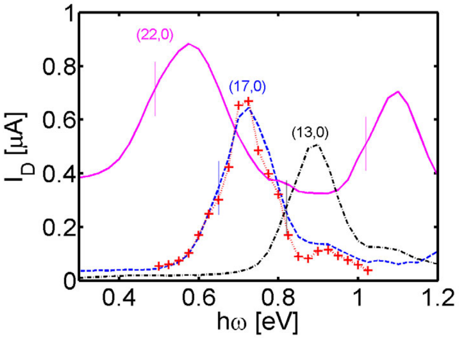

Fig.6.3 The source-drain current versus the photon energy in for a (22,0) CNT with E_g≈0.49eV (the solid line), a (17,0) CNT with E_g≈0.63eV (the dashed line), and a (13,0) CNT with E_g≈0.82eV (the dash-dot line) under the illumination intensity of $10^7 W/cm^2$ at V_G=V_D/2=0.2V in the presence of electron-phonon coupling. For comparison, the dotted line with crosses shows the current of the (17,0) CNT without electron-phonon coupling . The vertical bars show the subband gaps.

The effect of electron-phonon coupling on the photocurrent is examined in more detail next. The dotted line with symbols in Fig. 6.3 plots the photocurrent without electron-photon coupling for the (17,0) CNT, in order to compare to that in the presence of phonon scattering (the dashed line). Electron-phonon coupling (i) slightly broadens the main photocurrent peak near $\hbar\omega_{IR} \approx 0.7eV$, (ii) smoothes the oscillations on the I_D vs. $\hbar\omega_{IR}$ curve, and (iii) increases I_D by about 10% at energies of about $\hbar\omega_{OP}$ above the main peak. Electron-phonon coupling reduces the carrier life time and broadens the singularities of the DOS at the edge of the one-dimensional subbands. As a result, the photocurrent peak near $\hbar\omega_{IR} \approx 0.7eV$ is slightly broadened. Electron-phonon coupling breaks coherent transport in the channel and washes out quantum interference effect. The oscillations in the I_D vs. $\hbar\omega_{IR}$ curve, therefore, are smoothened. Furthermore, the increase of the source-drain current in the presence of phonon scattering near $\hbar\omega_{IR} \approx 0.7eV + \hbar\omega_{OP}$ is due to a phonon-assisted photocurrent [73].

7 Summary

A bottom-up simualtion approach based on the NEGF formalism has been developed for SWNT-FETs. The appoach has been applied to simulate DC characteristics, high-frequcncy peformance limits, and optoelectronic characteristics of SWNT-FETs. The DC simulation has matured to such a point that the measured I-V characteristics can be quantitatively described by device simulation [29]. Device simulation has been playing an important role in understanding experiments and suggesting design optimizations for SWNT-FETs. Many challenges, however, still remains. Although SWNT-FETs are being extensively explored for electronics applications, the first application may be in the area that large scale integration is less important (such as sensors[74, 75]). Extending the approach to simulate new device applications beyond CMOS, such as CNT sensors, is necessary. The Kondo effect and single electron charging [76] have been observed in SWNT-FETs. The effects are especially important at low temperatures. The current NEGF approach is limited to a single particle picture and a mean field theory. In order to capture these effects, extending the approach to treat strong electron-electron correlation is required. The high-frequency characteristics have been simulated based on quasi-static approximation. In order to capture non-quasi-static effects, a time-dependent transport formalism needs to be used. Excitons can qualitatively change the device optoelectronic characteristics. Treating excitons in device simulations imposes another challenge. The field of CNT device simulation has benefited from the rapid progress of experiments in the last decade. We expect that close interaction between theorists and experimentalists continues to play an important role in addressing these challenges in the future.

Acknowledgement

The authors would like to thank their collaborators, A. Javey, H. Dai, S. Datta, M. Alam, M. P. Anantram, S. Hasan, S. Koswatta, N. Neophytou, Y. Yoon, and Y. Ouyang, who contributed to the work described here.

REFERENCES

[1] P. Avouris, J. Appenzeller, R. Martel, and S. J. Wind, "Carbon nanotube electronics," *Proceedings of the IEEE*, vol. 91, pp. 1772-1784, 2003.

[2] P. L. McEuen, M. S. Fuhrer, and H. K. Park, "Single-walled carbon nanotube electronics," *IEEE Transactions on Nanotechnology*, vol. 1, pp. 78-85, 2002.

[3] S. Iijima and T. Ichihashi, "Single-Shell Carbon Nanotubes of 1-Nm Diameter," *Nature*, vol. 363, pp. 603-605, 1993.

[4] R. Saito, G. Dresselhaus, and M. S. Dresselhaus, *Physical properties of carbon nanotubes*. London: Imperial College Press, 1998.

[5] J. Appenzeller, Y. M. Lin, J. Knoch, Z. H. Chen, and P. Avouris, "Comparing carbon nanotube transistors - The ideal choice: A novel tunneling device design," *IEEE Transactions on Electron Devices*, vol. 52, pp. 2568-2576, 2005.

[6] M. P. Anantram, "Current-carrying capacity of carbon nanotubes," *Physical Review B*, vol. 62, pp. R4837-R4840, 2000.

[7] G. Pennington and N. Goldsman, "Semiclassical transport and phonon scattering of electrons in semiconducting carbon nanotubes," *Physical Review B*, vol. 68, pp. 045426, 2003.

[8] D. L. John, L. C. Castro, J. Clifford, and D. L. Pulfrey, "Electrostatics of coaxial Schottky-barrier nanotube field-effect transistors," *IEEE Transactions on Nanotechnology*, vol. 2, pp. 175-180, 2003.

[9] K. Alam and R. Lake, "Performance of 2 nm gate length carbon nanotube field-effect transistors with source/drain underlaps," *Applied Physics Letters*, vol. 87, pp. -, 2005.

[10] G. Flori, G. Iannaccone, and G. Klimeck, "Performance of Carbon Nanotube Field-Effect Transistors with Doped Source and Drain Extensions and Arbitrary Geometry," *IEDM Tech. Dig.*, vol. 2005, pp. 529, 2005.

[11] T. S. Xia, L. F. Register, and S. K. Banerjee, "Quantum transport in carbon nanotube transistors: Complex band structure effects," *Journal of Applied Physics*, vol. 95, pp. 1597-1599, 2004.

[12] Y. Q. Xue and M. A. Ratner, "Scaling analysis of electron transport through metal-semiconducting carbon nanotube interfaces: Evolution from the molecular limit to the bulk limit," *Physical Review B*, vol. 70, pp. -, 2004.

[13] J. Guo, M. Lundstrom, and S. Datta, "Performance projections for ballistic carbon nanotube field-effect transistors," *Applied Physics Letters*, vol. 80, pp. 3192-3194, 2002.

[14] P. J. Burke, "AC performance of nanoelectronics: towards a ballistic THz nanotube transistor," *Solid-State Electronics*, vol. 48, pp. 1981-1986, 2004.

[15] A. Verma, M. Z. Kauser, and P. P. Ruden, "Effects of radial breathing mode phonons on charge transport in semiconducting zigzag carbon nanotubes," *Applied Physics Letters*, vol. 87, pp. -, 2005.

[16] V. Perebeinos, J. Tersoff, and P. Avouris, "Electron-phonon interaction and transport in semiconducting carbon nanotubes," *Physical Review Letters*, vol. 94, pp. 027402, 2005.

[17] S. Datta, *Electronic transport in mesoscopic systems*. Cambridge, UK: Cambridge University Press, 1995.

[18] S. Datta, "Nanoscale device modeling: the Green's function method," *Superlattices and Microstructures*, vol. 28, pp. 253-278, 2000.

[19] S. Datta, *Quantum transport : atom to transistor*. Cambridge, UK ; New York: Cambridge University Press, 2005.

[20] R. Lake, G. Klimeck, R. C. Bowen, and D. Jovanovic, "Single and multiband modeling of quantum electron transport through layered semiconductor devices," *Journal of Applied Physics*, vol. 81, pp. 7845-7869, 1997.

[21] J. Guo, S. Koswatta, N. Neophytou, and M. Lundstrom, "Carbon Nanotube Field-Effect Transistors," *International Journal of High Speed Electronics and Systems*, vol. in press, 2006.

[22] D. Tomanek, S. G. Louie, H. J. Mamin, D. W. Abraham, R. E. Thomson, E. Ganz, and J. Clarke, "Theory and Observation of Highly Asymmetric Atomic-Structure in Scanning-Tunneling-Microscopy Images of Graphite," *Physical Review B*, vol. 35, pp. 7790-7793, 1987.

[23] J. Cerda and F. Soria, "Accurate and transferable extended Huckel-type tight-binding parameters," *Physical Review B*, vol. 61, pp. 7965-7971, 2000.

[24] X. Blase, L. X. Benedict, E. L. Shirley, and S. G. Louie, "Hybridization Effects and Metallicity in Small Radius Carbon Nanotubes," *Physical Review Letters*, vol. 72, pp. 1878-1881, 1994.

[25] A. Svizhenko, M. P. Anantram, T. R. Govindan, B. Biegel, and R. Venugopal, "Two-dimensional quantum mechanical modeling of nanotransistors," *Journal of Applied Physics*, vol. 91, pp. 2343-2354, 2002.

[26] J. Guo, S. Datta, M. Lundstrom, and M. P. Anantram, "Toward multi-scale modeling of carbon nanotube transistors," *the Interna-*

tional Journal on Multiscale Computer Engineering, vol. 2, pp. 257-277, 2004.

[27] N. Neophytou, D. Kienle, E. Polizzi, and M. P. Anantram, "Influence of defects on nanotube transistor performance," *Applied Physics Letters*, vol. 88, pp. -, 2006.

[28] Z. H. Chen, J. Appenzeller, J. Knoch, Y. M. Lin, and P. Avouris, "The role of metal-nanotube contact in the performance of carbon nanotube field-effect transistors," *Nano Letters*, vol. 5, pp. 1497-1502, 2005.

[29] A. Javey, J. Guo, D. B. Farmer, Q. Wang, E. Yenilmez, R. G. Gordon, M. Lundstrom, and H. J. Dai, "Self-aligned ballistic molecular transistors and electrically parallel nanotube arrays," *Nano Letters*, vol. 4, pp. 1319-1322, 2004.

[30] S. Heinze, J. Tersoff, R. Martel, V. Derycke, J. Appenzeller, and P. Avouris, "Carbon nanotubes as Schottky barrier transistors," *Physical Review Letters*, vol. 89, pp. 106801, 2002.

[31] J. Appenzeller, J. Knoch, V. Derycke, R. Martel, S. Wind, and P. Avouris, "Field-modulated carrier transport in carbon nanotube transistors," *Physical Review Letters*, vol. 89, pp. 126801, 2002.

[32] A. Javey, J. Guo, D. B. Farmer, Q. Wang, D. W. Wang, R. G. Gordon, M. Lundstrom, and H. J. Dai, "Carbon nanotube field-effect transistors with integrated ohmic contacts and high-k gate dielectrics," *Nano Letters*, vol. 4, pp. 447-450, 2004.

[33] J. Chen, C. Klinke, A. Afzali, and P. Avouris, "Self-aligned carbon nanotube transistors with charge transfer doping," *Applied Physics Letters*, vol. 86, pp. 123108, 2005.

[34] Y. M. Lin, J. Appenzeller, and P. Avouris, "Novel Carbon Nantoube FET Design with Tunable Polarity," *IEDM Tech. Dig.*, vol. San Francisco, CA, pp. 687-690, 2004.

[35] M. Radosavljevic, S. Heinze, J. Tersoff, and P. Avouris, "Drain voltage scaling in carbon nanotube transistors," *Applied Physics Letters*, vol. 83, pp. 2435-2437, 2003.

[36] J. Guo, S. Datta, and M. Lundstrom, "A numerical study of scaling issues for Schottky-Barrier carbon nanotube transistors," *IEEE Transactions on Electron Devices*, vol. 51, pp. 172-177, 2004.

[37] J. Guo, J. Wang, E. Polizzi, S. Datta, and M. Lundstrom, "Electrostatics of nanowire transistors," *IEEE Transactions on Nanotechnology*, vol. 2, pp. 329-334, 2003.

[38] Z. H. Chen, J. Appenzeller, Y. M. Lin, J. Sippel-Oakley, A. G. Rinzler, J. Y. Tang, S. J. Wind, P. M. Solomon, and P. Avouris, "An integrated logic circuit assembled on a single carbon nanotube," *Science*, vol. 311, pp. 1735-1735, 2006.

[39] A. Javey, J. Guo, Q. Wang, M. Lundstrom, and H. J. Dai, "Ballistic carbon nanotube field-effect transistors," *Nature*, vol. 424, pp. 654-657, 2003.

[40] J. Guo and M. S. Lundstrom, "A computational study of thin-body, double-gate, Schottky barrier MOSFETs," *IEEE Transactions on Electron Devices*, vol. 49, pp. 1897-1902, 2002.

[41] T. Durkop, B. M. Kim, and M. S. Fuhrer, "Properties and applications of high-mobility semiconducting nanotubes," *Journal of Physics-Condensed Matter*, vol. 16, pp. R553-R580, 2004.

[42] X. J. Zhou, J. Y. Park, S. M. Huang, J. Liu, and P. L. McEuen, "Band structure, phonon scattering, and the performance limit of single-walled carbon nanotube transistors," *Physical Review Letters*, vol. 95, pp. 146805, 2005.

[43] Z. Yao, C. L. Kane, and C. Dekker, "High-field electrical transport in single-wall carbon nanotubes," *Physical Review Letters*, vol. 84, pp. 2941-2944, 2000.

[44] J. Y. Park, S. Rosenblatt, Y. Yaish, V. Sazonova, H. Ustunel, S. Braig, T. A. Arias, P. W. Brouwer, and P. L. McEuen, "Electron-phonon scattering in metallic single-walled carbon nanotubes," *Nano Letters*, vol. 4, pp. 517-520, 2004.

[45] A. Javey, J. Guo, M. Paulsson, Q. Wang, D. Mann, M. Lundstrom, and H. J. Dai, "High-field quasiballistic transport in short carbon nanotubes," *Physical Review Letters*, vol. 92, pp. 106804, 2004.

[46] J. Guo, "A quantum-mechanical treatment of phonon scattering in carbon nanotube transistors," *Journal of Applied Physics*, vol. 98, pp. 063519, 2005.

[47] J. Guo and M. Lundstrom, "Role of Phonon Scattering in Carbon Nanotube Field-Effect Transistors," *Applied Physics Letters*, vol. 86, pp. 193103, 2005.

[48] S. Koswatta, S. Hasan, M. Lundstrom, M. P. Anantram, and D. E. Nikonov, "Ballisticity of nanotube FETs: role of phonon energy and gate bias," vol. 89, 023125, 2006.

[49] S. O. Koswatta, M. S. Lundstrom, M. P. Anantram, and D. E. Nikonov, "Simulation of phonon-assisted band-to-band tunneling in carbon nanotube field-effect transistors," *Applied Physics Letters*, vol. 87, pp. 253107, 2005.

[50] A. Svizhenko and M. P. Anantram, "Role of scattering in nanotransistors," *IEEE Transactions on Electron Devices*, vol. 50, pp. 1459-1466, 2003.

[51] M. S. Fuhrer, B. M. Kim, T. Durkop, T. Brintlinger, and E. Cobas, "High mobility semiconducting nanotubes for nanoelectronics.,"

Abstracts of Papers of the American Chemical Society, vol. 227, pp. U266-U266, 2004.

[52] J. Appenzeller and D. J. Frank, "Frequency dependent characterization of transport properties in carbon nanotube transistors," *Applied Physics Letters*, vol. 84, pp. 1771-1773, 2004.

[53] D. J. Frank and J. Appenzeller, "High-frequency response in carbon nanotube field-effect transistors," *IEEE Electron Device Letters*, vol. 25, pp. 34-36, 2004.

[54] S. D. Li, Z. Yu, S. F. Yen, W. C. Tang, and P. J. Burke, "Carbon nanotube transistor operation at 2.6 GHz," *Nano Letters*, vol. 4, pp. 753-756, 2004.

[55] X. Huo, M. Zhang, P. C. H. Chan, Q. Liang, and Z. K. Tang, "High-frequency S parameters characterization of back-gate carbon nantoube field-effect transistors," *IEDM Tech. Dig.*, vol. San Francisco, CA, pp. 691-694, 2004.

[56] S. Rosenblatt, H. Lin, V. Sazonova, S. Tiwari, and P. L. McEuen, "Mixing at 50GHz Using a Single-Walled Carbon Nanotube Transistor," *Applied Physics Letters*, vol. 87, pp. 153111, 2005.

[57] L. C. Castro, D. L. John, D. L. Pulfrey, M. Pourfath, A. Gehring, and K. H., "Method for predicting fT for Carbon Nanotube FETs," *IEEE Trans. Nanotechnology*, vol. 4, pp. 699-704, 2005.

[58] S. Hasan, S. Salahuddin, M. Vaidyanathan, and A. A. Alam, "High-frequency performance projections for ballistic carbon-nanotube transistors," *Ieee Transactions on Nanotechnology*, vol. 5, pp. 14-22, 2006.

[59] J. Guo, S. Hasan, A. Javey, G. Bosman, and M. Lundstrom, "Assessment of high-frequency performance potential of carbon nanotube transistors," *IEEE Transactions on Nanotechnology*, vol. 4, pp. 715-721, 2005.

[60] Y. Yoon, Y. Ouyang, and J. Guo, "Effect of Phonon Scattering on Intrisic Delay and Cut-Off Frequency of CNTFETs," *in press, IEEE Trans. on Electron Devices*, 2006.

[61] A. Rahman, J. Guo, S. Datta, and M. S. Lundstrom, "Theory of ballistic nanotransistors," *Ieee Transactions on Electron Devices*, vol. 50, pp. 1853-1864, 2003.

[62] J. A. Misewich, R. Martel, P. Avouris, J. C. Tsang, S. Heinze, and J. Tersoff, "Electrically induced optical emission from a carbon nanotube FET," *Science*, vol. 300, pp. 783-786, 2003.

[63] M. Freitag, J. Chen, J. Tersoff, J. C. Tsang, Q. Fu, J. Liu, and P. Avouris, "Mobile ambipolar domain in carbon-nanotube infrared emitters," *Physical Review Letters*, vol. 93, pp. 076803, 2004.

[64] M. Freitag, Y. Martin, J. A. Misewich, R. Martel, and P. H. Avouris, "Photoconductivity of single carbon nanotubes," *Nano Letters*, vol. 3, pp. 1067-1071, 2003.

[65] M. Freitag, V. Perebeinos, J. Chen, A. Stein, J. C. Tsang, J. A. Misewich, R. Martel, and P. Avouris, "Hot carrier electroluminescence from a single carbon nanotube," *Nano Letters*, vol. 4, pp. 1063-1066, 2004.

[66] M. S. Arnold, J. E. Sharping, S. I. Stupp, P. Kumar, and M. C. Hersam, "Band gap photobleaching in isolated single-walled carbon nanotubes," *Nano Letters*, vol. 3, pp. 1549-1554, 2003.

[67] F. Wang, G. Dukovic, L. E. Brus, and T. F. Heinz, "Time-resolved fluorescence of carbon nanotubes and its implication for radiative lifetimes," *Physical Review Letters*, vol. 92, pp. 177401, 2004.

[68] Z. C. Wu, Z. H. Chen, X. Du, J. M. Logan, J. Sippel, M. Nikolou, K. Kamaras, J. R. Reynolds, D. B. Tanner, A. F. Hebard, and A. G. Rinzler, "Transparent, conductive carbon nanotube films," *Science*, vol. 305, pp. 1273-1276, 2004.

[69] S. Zaric, G. N. Ostojic, J. Kono, J. Shaver, V. C. Moore, M. S. Strano, R. H. Hauge, R. E. Smalley, and X. Wei, "Optical signatures of the Aharonov-Bohm phase in single-walled carbon nanotubes," *Science*, vol. 304, pp. 1129-1131, 2004.

[70] J. Guo, M. A. Alam, and Y. Yoon, "Theoretical investigation on photoconductivity of single intrinsic carbon nanotubes," *Applied Physics Letters*, vol. 88, pp. 133111, 2006.

[71] V. Perebeinos, J. Tersoff, and P. Avouris, "Scaling of excitons in carbon nanotubes," *Physical Review Letters*, vol. 92, pp. 257402, 2004.

[72] D. A. Stewart and F. Leonard, "Photocurrents in nanotube junctions," *Physical Review Letters*, vol. 93, pp. 107401, 2004.

[73] V. Perebeinos, J. Tersoff, and P. Avouris, "Effect of exciton-phonon coupling in the calculated optical absorption of carbon nanotubes," *Physical Review Letters*, vol. 94, pp. -, 2005.

[74] J. Kong, N. R. Franklin, C. W. Zhou, M. G. Chapline, S. Peng, K. J. Cho, and H. J. Dai, "Nanotube molecular wires as chemical sensors," *Science*, vol. 287, pp. 622-625, 2000.

[75] R. Chen, Y. Zhang, D. Wang, and H. Dai, "Non-Covalent Sidewall Functionalization of Single-Walled Carbon Nanotubes for Protein Immobilization," *J. Am. Chem. Soc.*, vol. 123, pp. 3838-3839, 2001.

[76] H. W. C. Postma, T. Teepen, Z. Yao, M. Grifoni, and C. Dekker, "Carbon nanotube single-electron transistors at room temperature," *Science*, vol. 293, pp. 76-79, 2001.